Sustainable Energy & Fuels

PAPER

View Article Online
View Journal | View Issue

Cite this: *Sustainable Energy Fuels*, 2019, **3**, 1225

Protecting effect of mass transport during electrochemical reduction of oxygenated carbon dioxide feedstocks†

Kindle Williams, Nathan Corbin, Joy Zeng, Nikifar Lazouski, Deng-Tao Yang and Karthish Manthiram *

Electrochemical CO_2 reduction is a promising path toward mitigating carbon emissions while also monetizing waste gas through chemicals production and storage of surplus renewable energy. However, deploying such a technology for use on industrial CO_2 sources requires an understanding of the effects that gas feed impurities have upon CO_2 reduction reaction (CO_2RR). In this work, we elucidate the impact of molecular oxygen on the network of reactions occurring in a CO_2 reduction system. Our findings indicate that for a planar, polycrystalline Au electrode in an aqueous environment, oxygen reduction current is limited by the transport characteristics specific to the cell geometry and solvent; as a result, mass transport confers a protective effect by mitigating the otherwise thermodynamically and kinetically favorable reduction of oxygen. The presence of oxygen does not appear to have a significant impact on either CO_2RR or hydrogen evolution partial currents, indicating that the mechanisms of reduction reactions involving oxygen are independent of CO_2RR and hydrogen evolution. Further, an electrokinetic mechanistic analysis indicates many feasible candidates for the rate-determining step of CO_2RR; there is no indication that the CO_2RR mechanism at $P_{CO_2} = 0.5$ atm is altered by the presence of oxygen, as the Tafel slopes (59 mV dec^{-1}) and reaction orders with respect to bicarbonate (0), CO_2 (~1.5), and protons (0 from lack of KIE) are consistent between systems with $P_{O_2} = 0$ atm and those with $P_{O_2} = 0.5$ atm. While this is promising for the robustness of CO_2RR to oxygen impurities in gas feeds, the ultimate design tradeoff when utilizing CO_2 sources containing oxygen is between the cost of separation processes and the corresponding cost of power inefficiency as a result of electrons lost to oxygen reduction. This represents a first step in understanding kinetic and transport considerations in the design of gas-impurity-tolerant CO_2 reduction systems.

Received 16th January 2019
Accepted 11th March 2019

DOI: 10.1039/c9se00024k

rsc.li/sustainable-energy

Introduction

With the rise of concern regarding carbon dioxide (CO_2) emissions, CO_2 valorization as a means of energy storage or chemicals production is an attractive pursuit. While round-trip efficiencies for energy storage technologies such as lithium ion batteries and pumped hydro power are greater than those for CO_2 electroreduction to fuels,[1] the generation of energy-dense chemicals allows for flexibility of energy recovery strategy as well as for product utilization in synthetic organic applications. CO_2 reduction reactions (CO_2RR) have been employed to reach products ranging from carbon monoxide (CO) and formate to more deeply-reduced products such as ethylene, methanol, and ethanol.[2–4] Generating such products from point sources of CO_2 may prove to be an attractive means of both curtailing and monetizing CO_2 emissions in the future.

A major limitation of existing studies of CO_2 electroreduction, however, is that almost all experiments conducted to date have utilized gas feeds of 99.9% or purer CO_2. Those investigations which have focused on dilute streams of CO_2 have so far mostly done so in the context of low-conversion molecular catalysts and inert gas impurities such as nitrogen (N_2).[5] If CO_2 reduction is ever to be practically employed, it may not be feasible – logistically or economically – to expect end-users of CO_2 reduction technology to supply feedstocks of high CO_2 purity. Some estimates have indicated that the purification of CO_2 from air (which currently contains ~400 ppm or 0.04% CO_2)[6] would cost roughly $1000 per metric ton CO_2 captured, while similar capture from the effluents of coal-fired power plants (containing 10–15% CO_2) would cost about $25–100 per metric ton CO_2.[7] A more promising study on the design of a system for direct CO_2 capture from air was able to decrease the cost of air capture to $94–232 per ton CO_2.[8] However, even this cost may prove prohibitive for the commercialization of

Department of Chemical Engineering, Massachusetts Institute of Technology, Cambridge, MA 02139, USA. E-mail: karthish@mit.edu

† Electronic supplementary information (ESI) available: In-depth materials & methods, discussion re: effects of O_2 at lower overpotentials, transient current decay phenomena, and kinetic rate law derivations. See DOI: 10.1039/c9se00024k

CO_2 reduction technology, as many technoeconomic analyses investigating CO_2 reduction viability rely on CO_2 capture costs being no more than \$30–60 per ton CO_2.[9,10] Therefore, it would be valuable for developed CO_2 reduction technologies to exhibit some degree of tolerance to gas feed impurities.

Previous studies involving non-inert impurities in CO_2 reduction streams have focused on the effects of NO_x, SO_x, and O_2 on CO_2RR at Cu cathodes.[11,12] In these contexts, O_2 was treated either as a species with the propensity to interfere with other impurities (*e.g.* by oxidizing poisoning sulfide ions),[11] or as a catalyst oxidant.[12] *Ex situ* catalyst characterization and changes in bulk product distribution were the primary metrics of the impurities' effects, whereas impacts on the electroreduction mechanisms occurring in the cell and the physical phenomena governing the feed impurities' behavior in these contexts were not explicitly treated. Thus, there is a need to build upon these efforts in order to ensure the catalysts being developed for CO_2 reduction today will be viable for implementation in the future.

In particular, an abundant and reactive impurity in most anticipated CO_2 feed streams is molecular oxygen (O_2). Oxygen-tolerant catalytic networks are increasingly being studied for hydrogen evolution; methods for minimizing O_2 competition include the development of bio-inspired catalytic pockets in order to exclude, photo-reduce, or otherwise steer molecular oxygen away from poisoning catalytic systems for proton reduction.[13] Platinum catalysts for the hydrogen evolution reaction (HER) seem to maintain current density to HER in the presence of 0.21 atm O_2;[13] however, the exact means by which this is possible have not been investigated. It is equally as important, if not more so, for the impact of O_2 on CO_2 reduction to be studied and mitigated, since O_2 may very well be a constituent of CO_2 reduction gas feeds.

The goal of the present work is to demonstrate the effects of the presence of oxygen on the network of reactions occurring during electrochemical CO_2 reduction on gold catalysts. Gold was chosen as a test catalyst due to its high activity toward CO_2 reduction and for ease of study due to its high selectivity toward only gas-phase products (CO and H_2).[2,4,14–18] Cultivating an understanding of oxygen's effect on such an electrocatalytic system will pave the way for the development of systems with tolerance toward a broader variety of gas-phase impurities characteristic of many CO_2 point sources, which may be required for industrially viable CO_2 reduction.

Results and discussion

Materials and methods

Electrochemical cell. A two-compartment cell design was used for CO_2 reduction experiments (Fig. S1†).[19] A full treatment of cell design and assembly can be found in the ESI (Sections S.2 and S.7†).

Catalyst, electrolyte, reference, and gas feed preparation. Gold foils were mechanically wet-polished using new 400-grit sandpaper for 3 minutes, sonicated in Milli-Q® water for 3–5 minutes, and dried with compressed nitrogen gas prior to insertion in the electrochemical cell. Unpolished platinum foil was used as the counter-electrode, and the two electrode compartments were separated by a Selemion™ AMV anion-exchange membrane. Sodium bicarbonate electrolytes were prepared by dissolving sodium carbonate into Milli-Q® water to yield solutions with carbonate molarities of 1/2 the desired bicarbonate molarity, followed by bubbling overnight using instrument-grade (99.99%) CO_2 to convert the carbonate to bicarbonate. A leak-free Ag/AgCl reference electrode was used, and was calibrated to a master Ag/AgCl reference in saturated KCl before each experiment. Gas feeds during experiments were mixed by combining research-grade (99.999%) CO_2, industrial-grade (99.7%) O_2, and house-supplied N_2 (the inert feed) in the appropriate ratios. Total gas flow was set to 10 sccm unless otherwise noted, and the pressure in the electrochemical cell remained at roughly 1 atm. Further details on materials and experiments can be found in ESI (Section S.7†).

Product characterization. While minor electroreduction products were detected through a combination of NMR spectroscopy and colorimetric assays (Section S.8†), the majority of confirmed products were detected through in-line gas chromatography (GC). An SRI MG #5 Model 8610C GC was set up to auto-sample gas effluent from the electrochemical cell during operation. Products were detected using both a flame ionization detector (FID) and a thermal conductivity detector (TCD). Full details of GC setup and calibration can be found in ESI (Section S.8†). GC samples taken at $t = 20$, 30, and 40 minutes during each electrolysis experiment were averaged for the data reported herein. Oxygen reduction reaction (ORR) current densities for most experiments were calculated from the balance of current after accounting for all detected products. The validity of this approach is confirmed both by lack of detectable liquid-phase products (Section S.8.2†) and by FE closure to 100% in the absence of oxygen.

Oxygen's effect on reactions in a CO_2RR cell

Initial experiments were conducted holding the partial pressure of CO_2 constant at 0.5 atm, while the pressure of O_2 was varied between 0 and 0.5 atm using N_2 as the balance. The effect of the oxygen partial pressure on partial current densities toward CO_2RR, HER, and ORR was quantified (Fig. 1). Results of this experiment conducted at different voltages can be found in ESI (Section S.9†).

As increasing amounts of oxygen were added to the gas feed, current toward ORR increased linearly while partial currents toward CO_2RR and HER remained roughly constant. This implies that ORR chemistry did not affect CO_2RR or HER catalysis. Further, it suggests the nature of the catalyst itself may have been unaffected by the presence of oxygen. It should be noted that there is somewhat larger uncertainty in the partial current measurements toward CO_2RR and HER, consistent with previous studies using foil electrodes.[20,21] This is because foil preparation by polishing introduces surface irregularities that cannot be easily replicated from run to run. However, the uncertainties expressed in the error bars of this figure are noticeably small for the ORR data points. This is indicative that

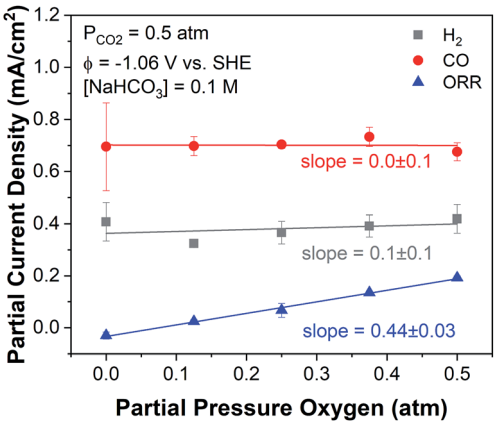

Fig. 1 Oxygen's effect on partial current densities of HER (black), CO_2RR (red), and ORR (blue) in a cell flowing 0.5 atm CO_2 and various amounts of O_2, with N_2 as inert balance. Experiments were conducted at −1.06 V *vs.* SHE (−0.65 V *vs.* RHE) in 0.1 M $NaHCO_3$, with each point in duplicate.

the quality of the foil preparation has no effect on ORR currents, and reinforces our confidence in the data.

At less reductive potentials and lower current densities, an apparent negative trend in both CO_2RR and HER current is observed (Fig. S11†). The fact that this trend is evident only at low overpotentials suggests either that oxygen interferes with these mechanisms in a distinct way at lower overpotentials, or that the effect of O_2 in the system is constant, but kept small on an absolute scale, therefore only showing up at low current densities.

To investigate why these trends hold true, the factors governing each reaction – namely, the kinetic *versus* transport control of ORR, as well as mechanistic aspects of CO_2RR and HER – were studied in the context of $P_{CO_2} = 0.5$ atm.

ORR under CO_2 reduction conditions on gold

CO_2RR, HER, and ORR can be described through the following respective equilibria on gold at pH 7:[2,22]

CO_2RR ($E^0 = -0.52$ V *vs.* SHE):

$$CO_2\ (aq) + H_2O\ (l) + 2e^- \rightleftharpoons CO\ (g) + 2OH^-\ (aq)$$

HER ($E^0 = -0.41$ V *vs.* SHE):

$$2H_2O\ (l) + 2e^- \rightleftharpoons H_2\ (g) + 2OH^-\ (aq)$$

$4e^-$ ORR ($E^0 = 0.82$ V *vs.* SHE):

$$O_2\ (aq) + 2H_2O\ (l) + 4e^- \rightleftharpoons 4OH^-\ (aq)$$

$2e^-$ ORR ($E^0 = 0.28$ V *vs.* SHE):

$$O_2\ (aq) + 2H_2O\ (l) + 2e^- \rightleftharpoons H_2O_2\ (l) + 2OH^-\ (aq)$$

Thermodynamics would dictate that at CO_2 reduction conditions that allow for the formation of CO, reducing oxygen is extremely favorable. Since the equilibrium potential for CO_2 reduction is roughly −0.52 V *vs.* SHE in neutral media, the cathode must be held at more reductive potentials than −0.52 V *vs.* SHE in order to achieve significant CO_2 reduction currents. It is reasonable to imagine that at greater than 1.3 V of overpotential, the rate of ORR may not be strictly dictated by kinetics. However, it was prudent to confirm this experimentally.

In this vein, cyclic voltammograms taken at $P_{CO_2} = 0.5$ atm were compared with and without a half-atmosphere of oxygen (Fig. 2A). It can be observed that at around 0.25 V *vs.* SHE, the onset of ORR occurs. This reduction current density plateaus at -0.26 mA cm^{-2} around −0.2 V *vs.* SHE. HER and CO_2RR onset, meanwhile, do not occur until the potential is swept down to almost −0.8 V *vs.* SHE. It is therefore concluded from this plot that ORR is transport-limited at the CO_2RR potentials of interest. This explains the phenomenon wherein ORR current is not impacted by changes introduced to the catalyst surface by polishing – the current is limited by diffusion.

For a planar electrode, assuming a stagnant boundary layer model (Fig. 2B), the formation of a linear species concentration profile at the catalyst surface leads to the expression:[23]

$$i_{\mathrm{lim},j} = -\frac{nFD_j c_{\mathrm{bulk},j}}{\delta_j} \quad (1)$$

where $i_{\mathrm{lim},j}$ represents the diffusion-limited current density for a reduction reaction involving species j, n is the number of electrons involved in the reduction, F is Faraday's constant, D_j is the diffusivity of species j, $c_{\mathrm{bulk},j}$ is the concentration of species j in the bulk of the solution (in turn dictated by Henry's law in the dilute limit), and δ_j is the mass transfer boundary layer thickness for species j. Because of the relative insolubility of oxygen in water – the Henry's law constant for O_2 is 0.0013 mol per kg per bar, compared to 0.034 mol per kg per bar for CO_2 [24] – the relative transport-limited current density of oxygen compared to carbon dioxide reduction in solution is quite low.

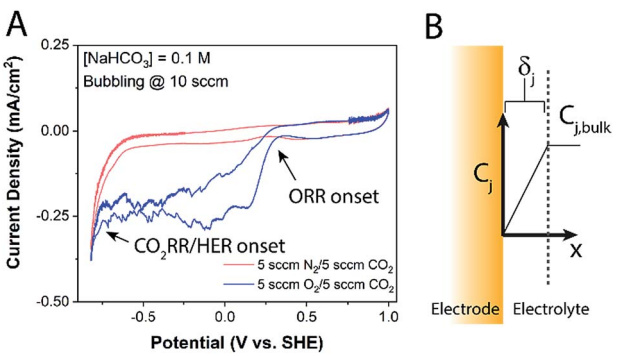

Fig. 2 (A) Modified CV scans (each is cycle #2 at a scan rate of 20 mV s^{-1}) showing the onset and transport limitation of ORR at potentials less reductive than the CO_2RR operating regime. Relevant transport conditions were simulated by maintaining gas bubbling at 10 sccm. (B) Conceptual sketch of the stagnant mass-transport boundary layer model.

To understand more about the mass-transport boundary layer in the cell, its thickness was determined by measuring the diffusion-limited current density of the ferricyanide ion and back-calculating its mass-transport boundary layer thickness using eqn (1).[25] A conversion was then applied to account for the difference in the diffusion coefficients of ferricyanide and gas-phase species such as CO_2 and O_2 (see ESI Section S.7.5†). For the transport of dissolved O_2 gas, the calculated boundary layer thickness was 200 ± 7 μm. Using the values $n = 4$ (see below), $D_{O_2} = 2.10 \times 10^{-5}$ cm^2 s^{-1},[26] and $C_{bulk,O_2} = 0.65$ mM at 0.5 atm,[24] the resulting prediction for the ORR diffusion-limited current density is 0.26 ± 0.01 mA cm^{-2}, in remarkable agreement with our voltammogram.

In addition, it was necessary to confirm which type of ORR was occurring under CO_2 reduction conditions. Gold is a known peroxide-forming ORR catalyst,[27] more typically implicated in selective H_2O_2 formation under acidic conditions,[28,29] whereas within the bicarbonate mass transport boundary layer, conditions should be slightly basic (up to pH 9–10, depending on the current density drawn).[30] Long-term experiments passing over 50C of charge were conducted in order to study the accumulation of ORR liquid-phase products; the colorimetric assay corresponding to the quantification of hydrogen peroxide in this electrolyte returned negative results, meaning that less than 10% of the oxygen being reduced is forming hydrogen peroxide (Section S.8.3†). We can therefore posit not only that ORR is transport-limited at relevant testing potentials, but also that it is primarily forming water. As water is the chief component of the electrolyte, the ORR products are not expected to interfere with any other catalytic cycles occurring in the cell.

Changes to mechanism of CO_2 reduction

To follow up on these observations, it was pertinent to interrogate the effect that oxygen's presence in the CO_2 reduction environment had on the HER and CO_2RR mechanisms, especially in the low-current density regime. As the kinetics of HER were difficult to probe – a kinetically interpretable Tafel slope for HER was never attained, consistent with previous observations[16] – the focus of this investigation was on the mechanism of CO_2RR. Probing the effect of oxygen in this context necessitates not only the study of the CO_2 reduction mechanism under oxygenated conditions, but also the study of the same mechanism at dilute concentrations and with no oxygen present, as most investigations of CO_2 reduction to this point have been conducted at 1 atm of CO_2.[15–18,31] To this end, a mechanistic study of CO_2 reduction was conducted.

Kinetic data were captured through Tafel analysis, bicarbonate dependence, CO_2 dependence, and kinetic isotope effect (KIE) experiments. The results are displayed and discussed below (Fig. 3).

Tafel slope. Tafel slopes were measured under 0.5 atm of CO_2 on Au, both with and without 0.5 atm O_2 (Fig. 3A). The Tafel slope for CO_2RR under the testing conditions without oxygen is 72 ± 4 mV dec^{-1}, while in the presence of oxygen the slope is 68 ± 6 mV dec^{-1}. The results presented are consistent with a theoretical 59 mV dec^{-1} Tafel slope. The resulting data were interpreted as being linear at potentials less reductive than −0.845 V *vs.* SHE. At potentials more reductive than this value, nonlinearities are observed which may be due to transport effects, mechanistic changes, or non-exponential kinetic response at high overpotentials.

The Tafel slope of 59 mV dec^{-1} indicates that a chemical step past the initial electron transfer to CO_2 is the rate-determining step (RDS) (see ESI Section S.11†). Subsequent experiments were designed to probe what this chemical step might be. Experiments were intended to probe purely the kinetics of the reaction and therefore were primarily conducted in the linear Tafel region – here selected as 300 mV overpotential, or −0.41 V *vs.* RHE in 0.1 M $NaHCO_3$ (−0.82 V *vs.* SHE).

Bicarbonate order dependence. One possibility for the RDS is the transfer of a proton from bicarbonate to the adsorbed CO_2 anion radical $\theta_{CO_2^{\cdot-}}$ to form θ_{COOH} (here θ is used to denote a surface adsorption site). The most straightforward way to test this RDS possibility is to conduct a bicarbonate order dependence test. This was done by varying the concentration of sodium bicarbonate in the electrolyte while holding the total solution ionic strength constant with sodium perchlorate. Perchlorate was regarded as an innocent bystander ion, while buffers such as phosphate were avoided due to their ability to poison the catalyst surface.[17] Further, the potential with respect to SHE rather than RHE was held constant, as this voltage is absolute in nature, and therefore represents the activity of the electron in the reaction – a factor which should be held constant when trying to probe the effects of a different reagent on the reaction rate. A full treatment of this topic can be found in the ESI (Section S.11†). These tests were performed at $P_{CO_2} = 0.5$ atm both with and without oxygen (Fig. 3B). In processing this data, partial current density results were normalized by the solubility of CO_2 – this controls for the secondary "salting-out" effect (see Section S.7.2†).[18,32]

While most conceivable CO_2RR mechanisms consistent with the Tafel data might have either a zeroth- or first-order dependence on bicarbonate, the slope in the bicarbonate plot suggests that CO_2RR is negatively impacted by increased bicarbonate concentrations. The slope without O_2 is −0.1 ± 0.2, while the slope with O_2 is −0.23 ± 0.05. This trend is especially true as we approach the solubility limit of sodium bicarbonate at roughly 1.2 M (see Section S.7.2†).[33] Results of the same experiment repeated with potassium bicarbonate, which is of a different purity than and nearly three times as soluble as the sodium salt, are shown in the ESI (Section S.7.2.2†). Because the potassium bicarbonate data yields a fairly clear zero-order dependence on bicarbonate, it is anticipated that the negative slope in the sodium case is the result of a secondary effect and that the reaction order in bicarbonate is 0.

CO_2 order dependence. Experiments probing the effect of P_{CO_2} in the inlet gas on CO_2RR current were conducted (Fig. 3C). It should be noted that changes in P_{CO_2} corresponded to bulk electrolyte pH changes; however, since bicarbonate order was found to be 0, this was regarded as having no convoluting effect on the CO_2 order dependence measurement. With slopes of 1.6 ± 0.2 and 1.2 ± 0.3 respectively for the cases with and without oxygen, the reaction order with respect to CO_2 can neither be

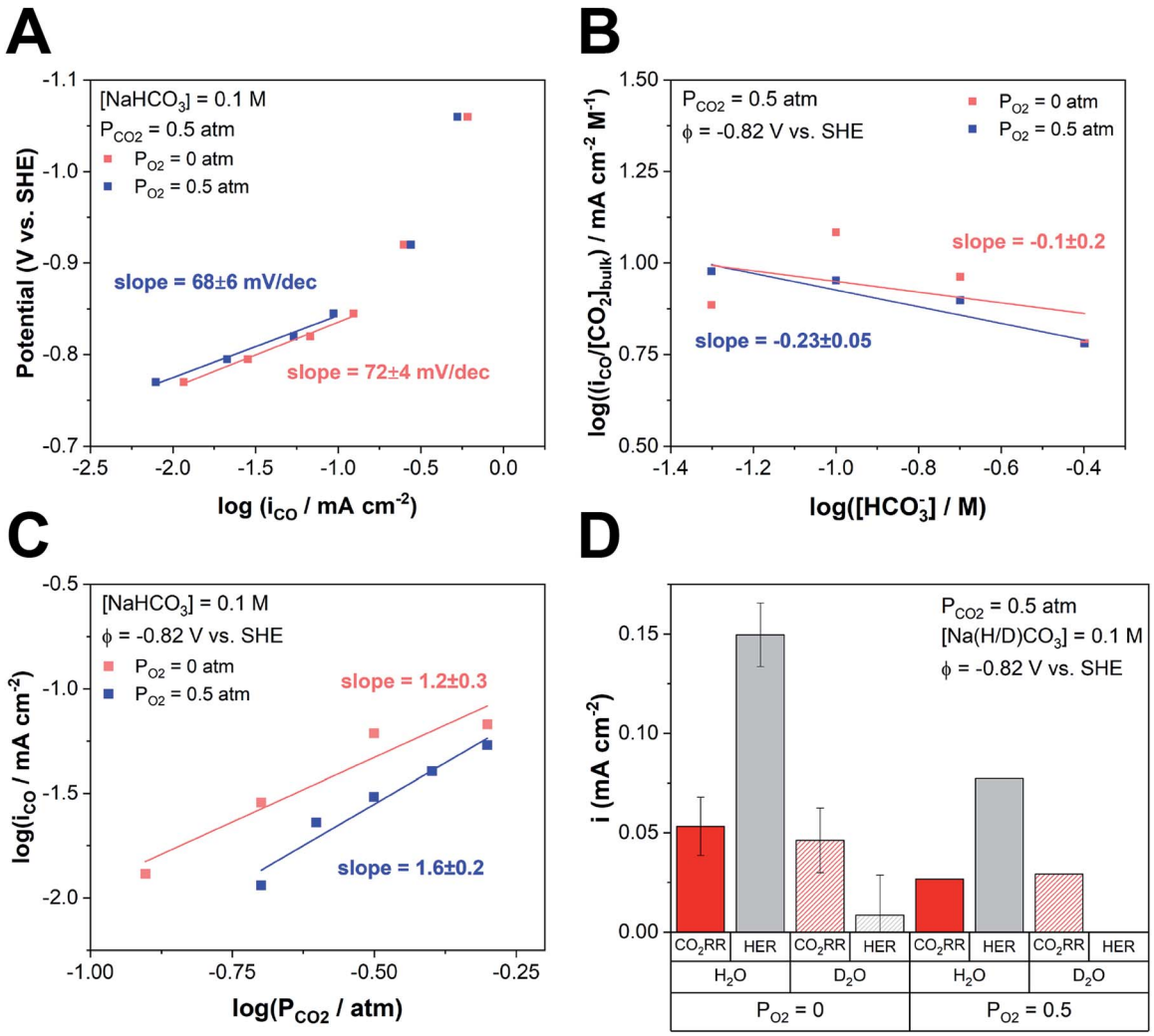

Fig. 3 Summary of CO_2RR kinetic data on polycrystalline Au for $P_{CO_2} = 0.5$ atm, both with and without 0.5 atm O_2. (A) Tafel slopes in 0.1 M $NaHCO_3$; (B) bicarbonate dependence at −0.82 V *vs.* SHE normalized by the bulk equilibrium concentration of CO_2; (C) P_{CO_2} dependence at −0.82 V *vs.* SHE in 0.1 M $NaHCO_3$; and (D) kinetic isotope effect for HER and CO_2RR at −0.82 V *vs.* SHE in 0.1 M $Na(H/D)CO_3$. Note that, consistent with the P_{O_2} effect data, there is a slight decrease of CO_2RR and HER currents when oxygen is present.

said to be 1 nor 2. In fact, it is possible that we are operating in a regime of mixed control, where the rates of different paths toward CO_2 reduction – one of which involves a solution-phase CO_2 accepting an oxygen atom from a surface-bound species to promote reduction of the bound species – are comparable. From these experiments alone, we cannot entirely rule out the possibility that the activity of CO_2 in solution may have a superlinear effect on current densities toward CO_2 reduction, although the slope here could also be due to changes in adsorbate coverage and other second-order effects.

Kinetic isotope effect. A proton involved in the RDS of CO_2RR need not come from the bicarbonate ion; protons are also plentiful in the aqueous solvent. To examine the role of protons in the RDS, it is useful to note that a proton transfer occurring in an RDS is normally subject to a kinetic isotope effect; that is, because the proton is so light, and because its vibrational mode is the coordinate along which the reaction proceeds, affecting the frequency of vibration by swapping out an H for a D can elucidate the participation of the H in the reaction. Thus, experiments were conducted in which the H_2O solvent was replaced by D_2O, with proper accounting for additional required drying, membrane soaking, and bubbler replacement in order to minimize adventitious H_2O sources (Fig. 3D) (Section S.7.3†).

It was shown that at the testing conditions, the KIE is negligible (KIE = $k_H/k_D = 1$ within error) for CO_2 reduction, while for HER the value of the KIE is greater than 10. This is suggestive that while the KIE could be considerable in this experiment given the participation of a proton in the RDS, the KIE is not observed, and therefore it is unlikely that a proton transfer is involved. Notably, KIE experiments have been known to lead to false negative conclusions, but only in very specific and rare instances.[34]

Mechanistic interpretation of kinetic data. Notably, the kinetic data obtained here in the context of $P_{CO_2} = 0.5$ atm differ from the outcomes presented in existing literature on CO_2RR mechanisms with $P_{CO_2} = 1$ atm.[17,18] We therefore present a list of

possible mechanisms, with a focus on those candidates which fit the Tafel slope data (Table 1). Derivations of rate laws and further discussion may be found in ESI (Section S.11†).

In these mechanisms, CO_2RR is regarded as proceeding through inner-sphere transformations. The mechanistic step X.1, representing an adsorptive electron transfer to CO_2, is regarded as the first step in each of the proposed mechanisms. While the list of mechanistic possibilities compiled here is not exhaustive, it encompasses many of the commonly reported mechanisms of CO_2 reduction to CO on Au, as well as a number of speculative possibilities.[31] In particular, excluded from this list are possibilities involving concerted proton-electron transfer (CPET). However, all mechanisms with CPET corresponding to initial CO_2 adsorption can also be collapsed down into the starting points represented by mechanistic steps C.2 and F.2, and therefore are also encompassed by this treatment.

The more commonly accepted intermediates for CO_2RR are implicated in mechanisms A and B. However, RDS candidates A.2 and B.2 are ruled out due to lack of bicarbonate dependence and KIE, respectively.

If we allow for the participation of surface sites or adsorbed species which are uncommon in the existing literature, then many RDS candidates remain (bolded options, Table 1). These include steps involving the formation of an Au–O bond, which we deem unlikely on the basis of gold's low oxophilicity; examples of this are θ_{COOH} dissociation into adsorbed CO and OH (mechanism C, excluded on the grounds of pH dependence) and the dissociation of adsorbed $CO_2^{\bullet-}$ into CO and an oxygen atom anion radical adsorbate (D.2). Mechanisms forming an Au–O bond can be avoided by instead invoking a cationic θ_{CO^+} adsorbate species, which seems only to have been described in metal complexes rather than on surfaces;[35,36] this is exemplified in mechanisms which exhibit the participation of CO_2 in the RDS (E.2) and the dissociation of the θ_{COOH} intermediate into charged species (mechanism F, excluded on the grounds of pH dependence). Further, under certain mathematical assumptions and allowing for the θ_{COOH^-} anion, the desorption of CO

Table 1 Postulated mechanisms of CO_2 reduction on gold under 0.5 atm CO_2[a17,31]

	RDS	Tafel slope form	Tafel slope at 298 K, $\beta = 0.5$	Acidic proton order	P_{CO_2} order	KIE?
X.1	$CO_2 + \theta + e^- \rightleftharpoons \theta_{CO_2^{\bullet-}}$	*2.3RT/βF*	*118*	*0*	*1*	*N*
A.2	$\theta_{CO_2^{\bullet-}} + HCO_3^- \rightleftharpoons \theta_{COOH} + CO_3^{2-}$	2.3*RT*/*F*	59	1	1	Y
A.3	$\theta_{COOH} + e^- \rightleftharpoons \theta + CO + OH^-$	2.3*RT*/(*β* + 1)*F*	39	0	1	N
B.2	$\theta_{CO_2^{\bullet-}} + H_2O \rightleftharpoons \theta_{COOH} + OH^-$	2.3*RT*/*F*	59	0	1	Y
B.3	$\theta_{COOH} + e^- \rightleftharpoons \theta + CO + OH^-$	2.3*RT*/(*β* + 1)*F*	39	0	1	N
C.2*	$\theta_{CO_2^{\bullet-}} + [H^+] \rightleftharpoons \theta_{COOH}$	2.3*RT*/*F*	59		1	Y
C.3	$\theta_{COOH} + \theta \rightleftharpoons \theta_{CO} + \theta_{OH}$	2.3*RT*/*F*	59	0	1	N
C.4	$\theta_{CO} \rightleftharpoons \theta + CO$	2.3*RT*/2*F*	30	0	1	N
D.2	$\boldsymbol{\theta_{CO_2^{\bullet-}} + \theta \rightleftharpoons \theta_{CO} + \theta_{O^{\bullet-}}}$	**2.3*RT*/*F***	**59**	**0**	**1**	**N**
D.3	$\theta_{CO} \rightleftharpoons \theta + CO$	2.3*RT*/2*F*	30	0	1	N
E.2	$\boldsymbol{\theta_{CO_2^{\bullet-}} + CO_2 \rightleftharpoons \theta_{CO^+} + CO_3^{2-}}$	**2.3*RT*/*F***	**59**	**0**	**2**	**N**
E.3	$\theta_{CO^+} + e^- \rightleftharpoons \theta + CO$	2.3*RT*/(*β* + 1)*F*	39	0	2	N
F.2*	$\theta_{CO_2^{\bullet-}} + [H^+] \rightleftharpoons \theta_{COOH}$	2.3*RT*/*F*	59		1	Y
F.3	$\theta_{COOH} \rightleftharpoons \theta_{CO^+} + OH^-$	2.3*RT*/*F*	59	0	1	N
F.4	$\theta_{CO^+} + e^- \rightleftharpoons \theta + CO$	2.3*RT*/(*β* + 1)*F*	39	0	1	N
G.1†	$HCO_3^- + \theta + e^- \rightleftharpoons \theta_H + CO_3^{2-}$					
G.2	$\theta_{CO_2^{\bullet-}} + \theta_H \rightleftharpoons \theta_{COOH^-} + \theta$	2.3*RT*/*F*	59‡	0	1	Y
G.3	$\boldsymbol{\theta_{COOH^-} \rightleftharpoons \theta + CO + OH^-}$	**2.3*RT*/*F***	**59‡**	**0**	**1**	**N**
H.2	$\boldsymbol{\theta_{CO_2^{\bullet-}} + \gamma \rightleftharpoons \theta + \gamma_{CO_2^{\bullet-}}}$	**2.3*RT*/*F***	**59**	**0**	**1**	**N**
H.n◇	—					

[a] Outcomes of experiments to probe the kinetics are listed next to each step in every postulated mechanism, under the circumstances that the step in question is the respective mechanism's rate-determining step (RDS). θ represents a catalytic active site on the Au electrode. β is the symmetry factor, interpreted as being 0.5. X.1 represents the first step in each of the proposed mechanisms. Bolded steps remain plausible RDS candidates after the kinetic investigation conducted here. *C.2 and F.2 are written such that any proton donor could in principle serve as the proton source, including water and bicarbonate. †G.1 is a separate mechanistic step also involved in the HER pathway. ‡Mechanism G requires the assumption that θ_H is dictated by equilibrium described by the Tafel step of HER. See derivation (S.11.4). ◇H.n steps could in principle be almost anything, including previously listed mechanisms. H.2 is simply the rearrangement of $CO_2^{\bullet-}$ on the surface to generate an intermediate which then reacts to form products. It does not necessarily require that γ differs from θ.

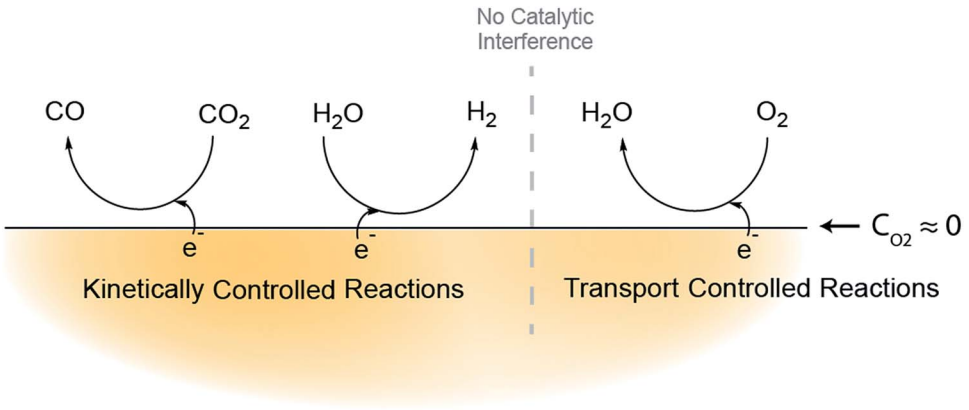

Scheme 1 Interactions between CO_2RR, HER, and ORR during cathodic polarization on a bulk Au surface.

(G.3) is an RDS that is consistent with the data. A conformation change of adsorbed $CO_2^{\bullet-}$ (H.2) may also serve as the RDS.

Accumulation of surface intermediates involved in these mechanisms could be assessed by use of FT-IR in order to further narrow down the mechanistic possibilities or develop new, more plausible hypotheses. For instance, a large IR band associated with θ_{CO} may indicate that this species has accumulated on the surface and is therefore the bottleneck in CO_2RR, supporting a CO desorption step as an RDS. The observation of such intermediates is currently a subject of debate.[16,18]

More relevant to the discussion of oxygen's effects, however, is the understanding of whether the mechanism of CO_2 reduction changes under oxygenated conditions in the electrochemical cell. The findings presented above suggest that so far, we have no reason to believe the mechanism of CO_2 reduction changes in the presence of oxygen. This is a promising result if we hope to develop oxygen-tolerant CO_2 reduction systems in the future.

Synthesizing the data into a picture of oxygen's interactions

Our understanding of the effect of ORR on the product distribution allows us to envision the interactions at the catalyst surface wherein the electrocatalytic steps involving CO_2 and HER are distinct from and unaffected by ORR intermediates and products (Scheme 1). In this conception of the relevant catalytic interactions, while the mechanisms of none of the individual reactions can be isolated, the chemistries of CO_2RR and HER *vs.* ORR are nonetheless distinct from one another.

Because oxygen is less soluble than CO_2 in aqueous electrolyte, transport provides a protecting effect against ORR. However, that does not mean that ORR even in this context is entirely benign. It is important to note that for practical design purposes, a high-rate CO_2 reduction reactor may need to operate under configurations such as a gas diffusion electrode (GDE) or a flowing-electrolyte design, wherein the length scales over which interfacial transport occurs are much smaller, and protecting effects of solubility are lessened. In such a scenario, the mechanistic analysis conducted here may not apply; further, power inefficiencies as a result of ORR may dominate economic considerations. Even in the context of the aqueous cell with a planar electrode reported here, assuming $CO_2 : O_2$ ratios typical of flue gas streams from natural gas power plants (roughly 1.67 : 1),[37] and assuming activity and selectivity to CO_2 matching those reported here at −1.06 V *vs.* SHE, roughly 12% of applied power would be lost to ORR. In the case that this value in a practical system is smaller than the equivalent power loss required to purify a CO_2 stream of oxygen, direct reduction of a mixed O_2/CO_2 stream may be a viable design option. The strategy to accept loss of power in a CO_2 electrolyzer could be viewed as complementary to other techniques which have been suggested for thermochemically reducing dilute oxygen impurities in CO_2-rich feedstocks using methane.[38]

Conclusions

The presence of oxygen was shown to not have a significant impact on the current toward CO_2 reduction at high current densities, largely due to the suppression of ORR by the transport characteristics of a flooded aqueous electrolysis system. The presence of oxygen has not to this point been implicated in affecting the mechanism of CO_2 reduction. While these are promising results for CO_2 reduction system design and scale-up, it is likely that ORR could become an economic consideration, with the design trade-off being between cost of CO_2 separation and power inefficiencies introduced by the presence of oxygen.

Future work should be dedicated toward developing a better understanding of the RDS of CO_2RR on gold, as well as conducting similar studies on more oxophilic metals. Further, for power efficiency purposes, it may prove economical to invest effort toward the design of an inherently oxygen-tolerant CO_2RR system through modulating transport parameters at the electrode surface.

Conflicts of interest

There are no conflicts to declare.

Acknowledgements

The authors would like to thank Zachary Schiffer, Kyoungsuk Jin, and Joseph Maalouf for their help and insightful feedback. We also thank the MIT Department of Chemistry Instrumentation Facility (DCIF) for the use of their NMR spectrometer. This work was funded by the MIT Energy Initiative (MITEI) Carbon Capture, Utilization, and Storage (CCUS) Center and the Advanced Concepts Committee at MIT Lincoln Laboratory.

References

1 I. E. Commission, *Electrical Energy Storage*, 2011.
2 Y. Hori, *Mod. Aspects Electrochem.*, 2008, vol. 42, pp. 89–189.
3 K. P. Kuhl, E. R. Cave, D. N. Abram and T. F. Jaramillo, *Energy Environ. Sci.*, 2012, **5**, 7050–7059.
4 K. P. Kuhl, T. Hatsukade, E. R. Cave, D. N. Abram, J. Kibsgaard and T. F. Jaramillo, *J. Am. Chem. Soc.*, 2014, **136**, 14107–14113.
5 H. Kumagai, T. Nishikawa, H. Koizumi, T. Yatsu, G. Sahara, Y. Yamazaki, Y. Tamaki and O. Ishitani, *Chem. Sci.*, 2019, **10**, 1597–1606.
6 E. S. R. L. US Department of Commerce, NOAA, ESRL Global Monitoring Division - Global Greenhouse Gas Reference Network, https://www.esrl.noaa.gov/gmd/ccgg/trends/, accessed 7 November 2018.
7 K. Z. House, A. C. Baclig, M. Ranjan, E. A. van Nierop, J. Wilcox and H. J. Herzog, *Proc. Natl. Acad. Sci. U. S. A.*, 2011, **108**, 20428–20433.
8 D. W. Keith, G. Holmes, D. St. Angelo and K. Heidel, *Joule*, 2018, **2**, 1–22.
9 O. S. Bushuyev, P. De Luna, C. T. Dinh, L. Tao, G. Saur, J. Van De Lagemaat, S. O. Kelley and E. H. Sargent, *Joule*, 2018, **2**, 825–832.
10 S. Verma, B. Kim, H. M. Jhong and S. Ma, 2016, 1972–1979.
11 Y. Zhai, L. Chiachiarelli and N. Sridhar, *ECS Trans.*, 2009, **19**, 11–13.
12 A. Engelbrecht, M. Hämmerle, R. Moos, M. Fleischer and G. Schmid, *Electrochim. Acta*, 2017, **224**, 642–648.
13 D. W. Wakerley and E. Reisner, *Energy Environ. Sci.*, 2015, **8**, 2283–2295.
14 E. R. Cave, J. H. Montoya, K. P. Kuhl, D. N. Abram, T. Hatsukade, C. Shi, C. Hahn, J. K. Nørskov and T. F. Jaramillo, *Phys. Chem. Chem. Phys.*, 2017, **19**, 15856–15863.
15 Y. Chen, C. W. Li and M. W. Kanan, *J. Am. Chem. Soc.*, 2012, **134**, 19969–19972.
16 A. Wuttig, M. Yaguchi, K. Motobayashi, M. Osawa and Y. Surendranath, *Proc. Natl. Acad. Sci. U. S. A.*, 2016, **113**, E4585–E4593.
17 A. Wuttig, Y. Yoon, J. Ryu and Y. Surendranath, *J. Am. Chem. Soc.*, 2017, **139**, 17109–17113.
18 M. Dunwell, Q. Lu, J. M. Heyes, J. Rosen, J. G. Chen, Y. Yan, F. Jiao and B. Xu, *J. Am. Chem. Soc.*, 2017, **139**, 3774–3783.
19 P. Lobaccaro, M. R. Singh, E. L. Clark, Y. Kwon, A. T. Bell and J. W. Ager, *Phys. Chem. Chem. Phys.*, 2016, **18**, 26777–26785.
20 T. Hatsukade, K. P. Kuhl, E. R. Cave, D. N. Abram and T. F. Jaramillo, *Phys. Chem. Chem. Phys.*, 2014, **16**, 13814–13819.
21 A. Wuttig and Y. Surendranath, *ACS Catal.*, 2015, **5**, 4479–4484.
22 Electrochemical Series – Alphabetical Listing, in *CRC Handbook of Chemistry and Physics*, ed. J. R. Rumble, CRC Press/Taylor & Francis, Boca Raton, FL, 99th edn, 2018, http://hbcponline.com/faces/documents/05_22/05_22_0017.xhtml.
23 W. M. Deen, *Analysis of Transport Phenomena*, Oxford University Press, 2nd edn, 2011.
24 U. S. D. of Commerce, *NIST Chemistry WebBook*, 2018, http://webbook.nist.gov/chemistry/%0A.
25 E. L. Clark, J. Resasco, A. Landers, J. Lin, L.-T. Chung, A. Walton, C. Hahn, T. F. Jaramillo and A. T. Bell, *ACS Catal.*, 2018, **8**, 6560–6570.
26 E. L. Cussler, *Diffusion: Mass Transfer in Fluid Systems*, 2nd edn, 1997.
27 M. T. M. Koper, *Chem. Sci.*, 2013, **4**, 2710–2723.
28 I. Srejić, M. Smiljanić, Z. Rakočević and S. Štrbac, *Int. J. Electrochem. Sci.*, 2016, **11**, 10436–10448.
29 X. Ge, A. Sumboja, D. Wuu, T. An, B. Li, F. W. T. Goh, T. S. A. Hor, Y. Zong and Z. Liu, *ACS Catal.*, 2015, **5**, 4643–4667.
30 N. Gupta, M. Gattrell and B. Macdougall, 2006, 161–172.
31 C. W. Lee, N. H. Cho, S. W. Im, M. S. Jee, Y. J. Hwang, B. K. Min and K. T. Nam, *J. Mater. Chem. A*, 2018, **6**, 14043–14057.
32 S. Weisenberger and A. Schumpe, *AIChE J.*, 1996, **42**, 298–300.
33 N. C. for B. Information, Sodium bicarbonate | $NaHCO_3$ - PubChem, https://pubchem.ncbi.nlm.nih.gov/compound/sodium_bicarbonate#section=Solubility.
34 M. T. Huynh, S. J. Mora, M. Villalba, M. E. Tejeda-Ferrari, P. A. Liddell, B. R. Cherry, A. L. Teillout, C. W. MacHan, C. P. Kubiak, D. Gust, T. A. Moore, S. Hammes-Schiffer and A. L. Moore, *ACS Cent. Sci.*, 2017, **3**, 372–380.
35 A. S. Goldman and K. Krogh-Jespersen, *J. Am. Chem. Soc.*, 1996, **118**, 12159–12166.
36 Q. Xu, *Coord. Chem. Rev.*, 2002, **231**, 83–108.
37 X. Xu, C. Song, R. Wincek, J. M. Andresen, B. G. Miller and A. W. Scaroni, *Fuel Chemistry Division Preprints*, 2003, **48**, 162–163.
38 H. Yang, A. Kuhn, Z. Chen and Y. Lu, *Energy Technol.*, 2018, DOI: 10.1002/ente.201800917.

